





Spectroscopic Imaging of the Sun with MeerKAT: Opening a New Frontier in Solar Physics

Devojyoti Kansabanik¹ , Surajit Mondal² , Divya Oberoi¹ , James O. Chibueze^{3,4,5} , N. E. Engelbrecht⁴ , R. D. Strauss⁴ ,
E. P. Kontar⁶ , G. J. J. Botha⁷ , P. J. Steyn⁴ , and Amoré E. Nel⁸ 

¹ National Centre for Radio Astrophysics, Tata Institute of Fundamental Research, S.P. Pune University Campus, Pune 411007, India; dkansabanik@ncra.tifr.res.in

² Center for Solar-Terrestrial Research, New Jersey Institute of Technology, 323 M L King Jr Boulevard, Newark, NJ 07102-1982, USA

³ Department of Mathematical Sciences, University of South Africa, Cnr Christian de Wet Rd and Pioneer Avenue, Florida Park, 1709, Roodepoort, South Africa

⁴ Centre for Space Research, Physics Department, North-West University, Potchefstroom 2520, South Africa

⁵ Department of Physics and Astronomy, Faculty of Physical Sciences, University of Nigeria, Carver Building, 1 University Road, Nsukka 410001, Nigeria

⁶ School of Physics and Astronomy, University of Glasgow, Glasgow, G12 8QQ, UK

⁷ Department of Mathematics, Physics, and Electrical Engineering, Northumbria University, Newcastle upon Tyne, NE1 8ST, UK

⁸ The South African National Space Agency, Hermanus, 7200, South Africa

Received 2023 October 6; revised 2023 November 2; accepted 2023 November 3; published 2024 January 17

Abstract

Solar radio emissions provide several unique diagnostics to estimate different physical parameters of the solar corona, which are otherwise simply inaccessible. However, imaging the highly dynamic solar coronal emissions spanning a large range of angular scales at radio wavelengths is extremely challenging. At gigahertz frequencies, MeerKAT radio telescope is possibly globally the best-suited instrument at present for providing high-fidelity spectroscopic snapshot solar images. Here, we present the first published spectroscopic images of the Sun made using the observations with MeerKAT in the 880–1670 MHz band. This work demonstrates the high fidelity of spectroscopic snapshot MeerKAT solar images through a comparison with simulated radio images at MeerKAT frequencies. The observed images show extremely good morphological similarities with the simulated images. Our analysis shows that below ~ 900 MHz MeerKAT images can recover essentially the entire flux density from the large angular-scale solar disk. Not surprisingly, at higher frequencies, the missing flux density can be as large as $\sim 50\%$. However, it can potentially be estimated and corrected for. We believe once solar observation with MeerKAT is commissioned, it will enable a host of novel studies, open the door to a large unexplored phase space with significant discovery potential, and also pave the way for solar science with the upcoming Square Kilometre Array-Mid telescope, of which MeerKAT is a precursor.

Unified Astronomy Thesaurus concepts: [Solar corona \(1483\)](#); [Solar radio emission \(1522\)](#); [Solar coronal radio emission \(1993\)](#); [Solar instruments \(1499\)](#); [Solar radio telescopes \(1523\)](#); [Radio interferometers \(1345\)](#)

1. Introduction

Since the discovery of solar radio emission (Reber 1944), the Sun has been studied in great detail in a wide range of frequencies spanning the range from a few kilohertz to several hundreds of gigahertz (e.g., Pick & Vilmer 2008; Gary 2023). Despite this long history of observations and studies, the Sun still harbors several mysteries. Improved observations from the new telescopes enabled by technological advances help solve these mysteries. At the same time, these new advancements probe the Sun in ways not possible earlier, and thus far, have invariably opened up a very rich discovery space. Interesting results coming from new instruments like the Solar Orbiter (Müller et al. 2020; García Marirrodriga et al. 2021), Parker Solar Probe (PSP; Raouafi et al. 2023), Daniel K. Inouye Solar Telescope (Rimmele et al. 2020; Rast et al. 2021), Murchison Widefield Array (MWA; Lonsdale et al. 2009; Tingay et al. 2013; Wayth et al. 2018), LOw Frequency ARray (LOFAR; van Haarlem et al. 2013), Expanded Owens Valley Solar Array (EOVSA; Gary et al. 2012), the NenuFAR (Zarka et al. 2018; Briand et al. 2022), Long Wavelength Array (Kassim et al. 2010), and the Owens Valley Long Wavelength Array

(Hallinan et al. 2023) are a testament to this. Except for EOVSA, these new-generation radio telescopes are not dedicated solar facilities, nonetheless, they have already been opening up large expanses of pristine unexplored phase space and making substantial contributions.

MeerKAT (Jonas & MeerKAT Team 2016; Chen et al. 2021) is a new-generation instrument located in the MeerKAT National Park in the Northern Cape of South Africa. It consists of 64 dishes, each 13.5 m in diameter. Each MeerKAT dish is equipped with a cryogenically cooled receiver, making it extremely sensitive. At present, MeerKAT has three observing bands—the UHF (580–1015 MHz), *L* (900–1670 MHz), and *S* (1750–3500 MHz) bands. The array is centrally condensed with about 39 dishes lying within 1 km and the remaining dishes distributed within a radius of ~ 8 km. This provides MeerKAT with extremely good surface brightness sensitivity and also allows the generation of radio images with an extremely high dynamic range (DR) and image fidelity (e.g., Heywood et al. 2022). The dense array layout of MeerKAT also implies that it has an excellent spectroscopic snapshot sampling in the Fourier plane (*uv*-plane) as shown in Figure 1. This leads to a very well-behaved point-spread-function (PSF), making MeerKAT well suited for high-DR spectroscopic snapshot imaging. This capability is extremely useful for solar studies at radio wavelengths, due to the rapid dynamics seen in solar radio emissions both along spectral and temporal dimensions (Nindos et al. 2021; Oberoi et al. 2023). There

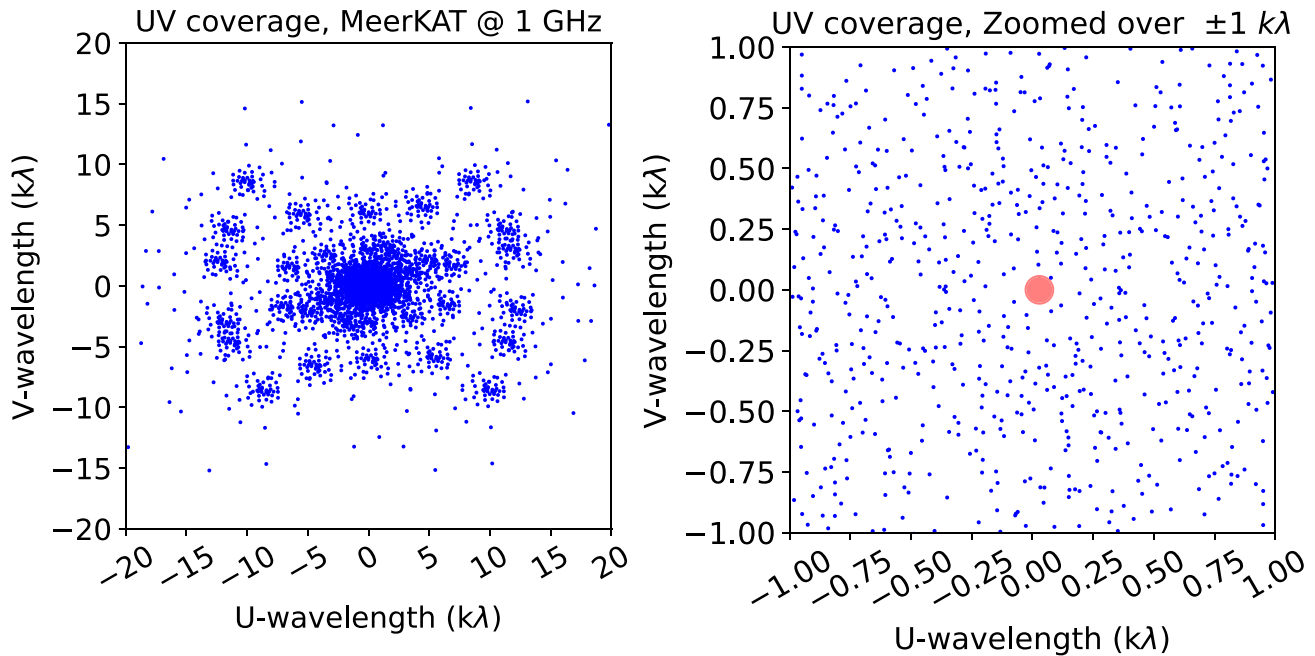


Figure 1. MeerKAT spectroscopic snapshot of uv -coverage. Left panel: spectroscopic snapshot of the uv -coverage of MeerKAT at 1 GHz. Right panel: same uv -coverage zoomed in over the central ± 1 $k\lambda$ region. The red circle corresponds to the uv -cell for a source with the size of the solar disk $32'$ in angular scale. Note that uv -points corresponding to even the shortest baseline lie outside this uv -cell.

are several avenues where high-DR snapshot imaging can lead to extraordinary science, ranging from the direct estimation of the magnetic field of the coronal mass ejections (CMEs) close to the Sun to studies of nonthermal emissions from extremely weak radio transients.

MeerKAT is a precursor instrument to the mid-frequency telescope of the upcoming Square Kilometre Array Observatory (SKAO; Dewdney et al. 2017; Santander-Vela et al. 2021), referred to as the SKA-Mid. Given its larger number of elements and longer baselines, SKA-Mid promises to be an even more capable instrument than MeerKAT and is expected to complete its construction phase sometime in 2028. The potential of the SKAO telescopes to provide major new insights into diverse aspects of solar physics is well recognized (Nakariakov et al. 2015; Nindos et al. 2019). Enabling solar science with MeerKAT is not only expected to be scientifically very rewarding in its own right, but it also lies on the critical path to enabling solar science with the SKA-Mid and forms a part of the motivation for this work. A similar approach with the SKA-Low precursor and pathfinder, MWA, and LOFAR, has yielded very rich solar science dividends (e.g., Oberoi et al. 2023).

There have been previous attempts to image the Sun with MeerKAT. While solar images have been generated successfully, these efforts have been driven primarily by technological demonstration objectives and have remained unpublished. Here we present the first detailed spectroscopic imaging study of the Sun with MeerKAT. Unlike standard astronomical observations, solar observations with any radio telescope pose several challenges. These challenges need to be addressed before MeerKAT can be used for solar observations. The primary reason behind this is that MeerKAT was designed for observing faint astronomical sources. To observe the Sun, the source with the highest flux density in the sky, the solar signal needs to be attenuated by many orders of magnitude to ensure that the astronomical signal stays in the linear regime of the instrument. However, the same attenuation cannot be used to observe the available calibrators as these sources are orders

of magnitude weaker than the Sun. In the absence of such calibrator observations, it is hard to estimate the instrumental gains and efforts that are ongoing toward solving these issues. Hence, we have used a different strategy to observe and image the Sun. Instead of pointing at the Sun, we pointed $\sim 2.5^\circ$ away to keep the Sun in the sidelobes of the primary beam to effectively attenuate the solar emissions. The sensitivity of MeerKAT is sufficient to image the Sun even when it is in the sidelobes of the primary beam. The availability of holographic measurements of the MeerKAT primary beam up to the second sidelobes (de Villiers & Cotton 2022; de Villiers 2023) allows us to obtain flux density calibrated solar images. We note that there are some shortcomings of this observing strategy. Among them, the nonuniform sensitivity over the solar disk due to the chromatic nature of the primary beam is the most important. Despite these shortcomings, our work substantiates the excellent spectroscopic snapshot imaging quality of MeerKAT solar data and showcases its potential for enabling excellent solar science.

This paper is organized as follows. Section 2 presents the details of the observations. Section 3 describes the data analysis procedure, including calibration, imaging, and primary beam correction. In Section 4, we present our results and demonstrate some early results achieved using these data. Finally, in Section 5, we conclude while giving a future outlook of MeerKAT solar observations.

2. Observations

The observations reported here were done as a part of a science verification observation under project ID SSV-20200709-SA-01. The raw visibilities for this project are available in the public domain through the SARAO data archive.⁹ The observations were carried out during the sixth perihelion passage of PSP (Fox 2017) from 2020 September 24

⁹ <https://archive.sarao.ac.za/>

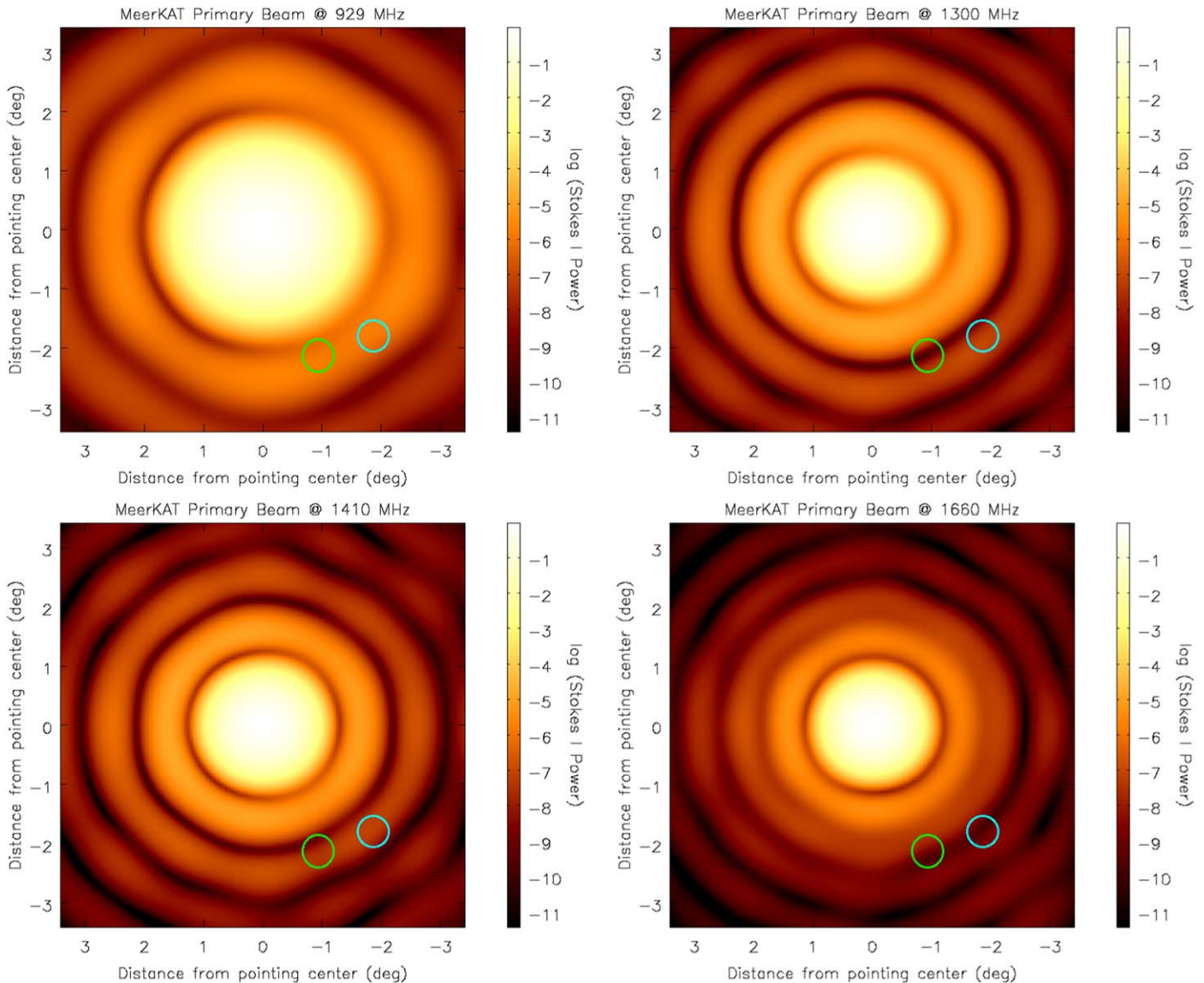


Figure 2. Locations of the Sun in the primary beam. Four different panels show MeerKAT holographic measured primary beam (de Villiers & Cotton 2022; de Villiers 2023) at frequencies ranging from 929–1660 MHz in increasing order. The cyan circle represents the location of the Sun on 2020 September 26 and the green circle represents that on 2020 September 27 for a particular observing scan. The position of the Sun changed azimuthally between different scans but lies at similar distances from the center of the primary beam.

to 2020 September 30. On each day, there are about 3 hr of observations centered around 10:30 UTC. In this paper, we present results from two of these epochs—2020 September 26 and 2020 September 27.

Observations were done covering 856–1712 MHz (usable frequency range 880–1670 MHz) with 32 K spectral channels and an 8 s temporal resolution. This provides us with data at about 26 kHz spectral resolution. The standard MeerKAT flux density calibrator, J0408-6545, was observed at the start of observations. J0408-6545 was used for bandpass and flux density calibration (hereafter referred to as fluxcal). J1239-1023 was used as a phase calibrator (hereafter referred to as phasecal) and observed between each consecutive solar scan. Since the Sun is a non-sidereal source, its R.A.–decl. changes with time. Hence, the pointing center was changed every 15 minutes. For all the pointings, the Sun was kept $\sim 2.5^\circ$ away from the pointing center. The position of the Sun in the primary beam for the particular scans from the two epochs analyzed

here are shown for four different frequencies in Figure 2. It turns out that at the lower part of the band, the Sun was in the first sidelobe of the primary beam, while it was in the second sidelobes or null at the higher parts of the band. This essentially makes the observations at the lower part of the observing band more sensitive than the high parts of the band. By keeping the Sun in the sidelobes of the primary beam, these observations can attenuate the solar signal by about -30 to -90 dB (in power), depending on the frequency. This is essential to keep the total power levels in the linear regime all through the signal chain.

3. Data Analysis

Since the observation does not fall under the standard astronomical observation category, we did not use SARAO Science Data Processor pipelines for the analysis. Instead, we did the analysis manually using Common Astronomy Software Application (CASA; McMullin et al. 2007; The CASA Team et al. 2022)

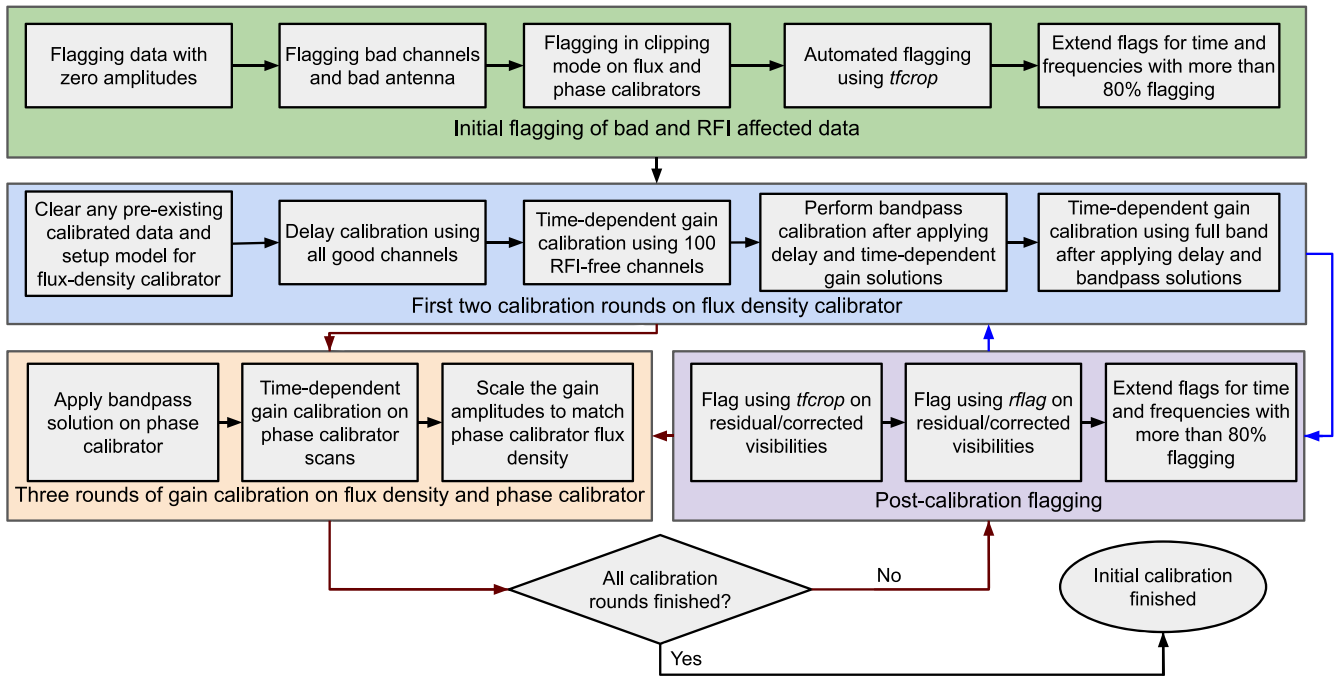


Figure 3. Flowchart describing the flagging and initial calibration procedure. The green box shows the steps of initial flagging on flux density and phase calibrators. The blue box shows the first two rounds of calibration steps on the flux density calibrator. The orange box shows the steps of the final three rounds of calibration on the phase calibrator. Each calibration round is followed by postcalibration flagging steps shown in the purple box. The first two cycles of calibration and postcalibration flagging are marked by blue arrows, and the last three rounds are marked by brown arrows.

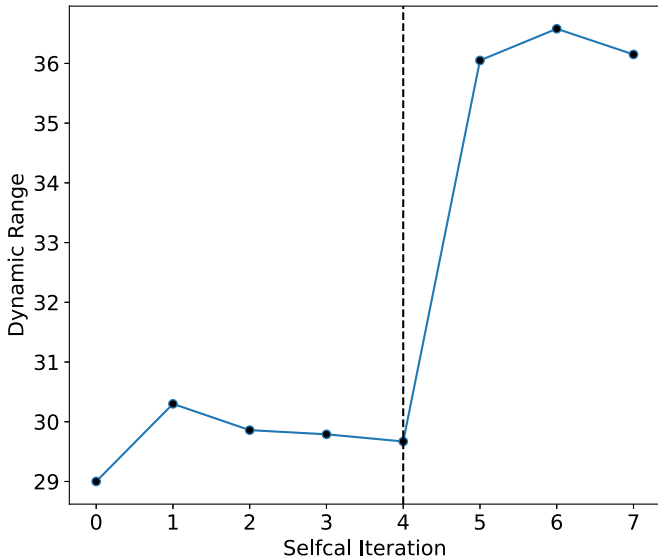


Figure 4. Changes in the imaging DR with self-calibration iterations for a single 20 MHz spectral slice centered at 929 MHz. The DR is estimated as the ratio of peak flux density and the rms noise close to the Sun. The black dashed line shows the iteration where amplitude-phase self-calibration is initiated.

for flagging and calibration and WSClean (Offringa et al. 2014) for imaging.

3.1. Flagging and Calibration

The flowchart for flagging and initial calibration procedures is shown in Figure 3. Initial flagging is performed to remove bad antennas, bad frequency channels, and other strong radio frequency interferences. Steps for initial flagging are marked by the green box in Figure 3. After that, initial calibration rounds are done using fluxcal and phasecal. A total of five rounds of

initial calibration were done. The steps of the first two rounds of calibration on fluxcal are shown in the blue box of the same figure. After the first two rounds of initial calibrations on fluxcal, the next three rounds of calibrations were done on both fluxcal and phasecal, the steps of which are shown in the orange box in the same figure. Each calibration round is followed by postcalibration flagging steps marked by the purple box in the same figure. Detailed procedures for the flagging and the initial calibration steps are discussed in Appendix A.

Once initial calibration and flagging are done, calibration solutions are applied to the solar scans, and self-calibration is performed. The Sun lies in the sidelobes of the MeerKAT primary beam, about 2.5° away from the nominal phase center at the center of the primary beam. To estimate and correct the complex gain toward the direction of the Sun, we first moved the phase center of the measured visibilities to the solar center before performing the self-calibration. Due to the chromatic nature of the primary beam, sensitivity across the solar disk varies with frequency. Also, being a nonsidereal source, the position of the Sun in the equatorial coordinate system changes with time. Hence, self-calibration is performed for each 20 MHz spectral chunk and 15 minute temporal chunk, separately. The DR of the image is determined as the ratio of the peak flux density of the Sun and the rms noise close to the Sun. DRs are estimated from images before the primary beam corrections. The improvement in the DR of the images of a 20 MHz spectral chunk centered at 929 MHz with self-calibration iterations is shown in Figure 4. To ensure the convergence of both phase-only and amplitude-phase self-calibration, we have compared the DRs of three consecutive rounds. When the DR of three consecutive rounds changes by less than 1, we assume self-calibration has converged. A detailed description of the

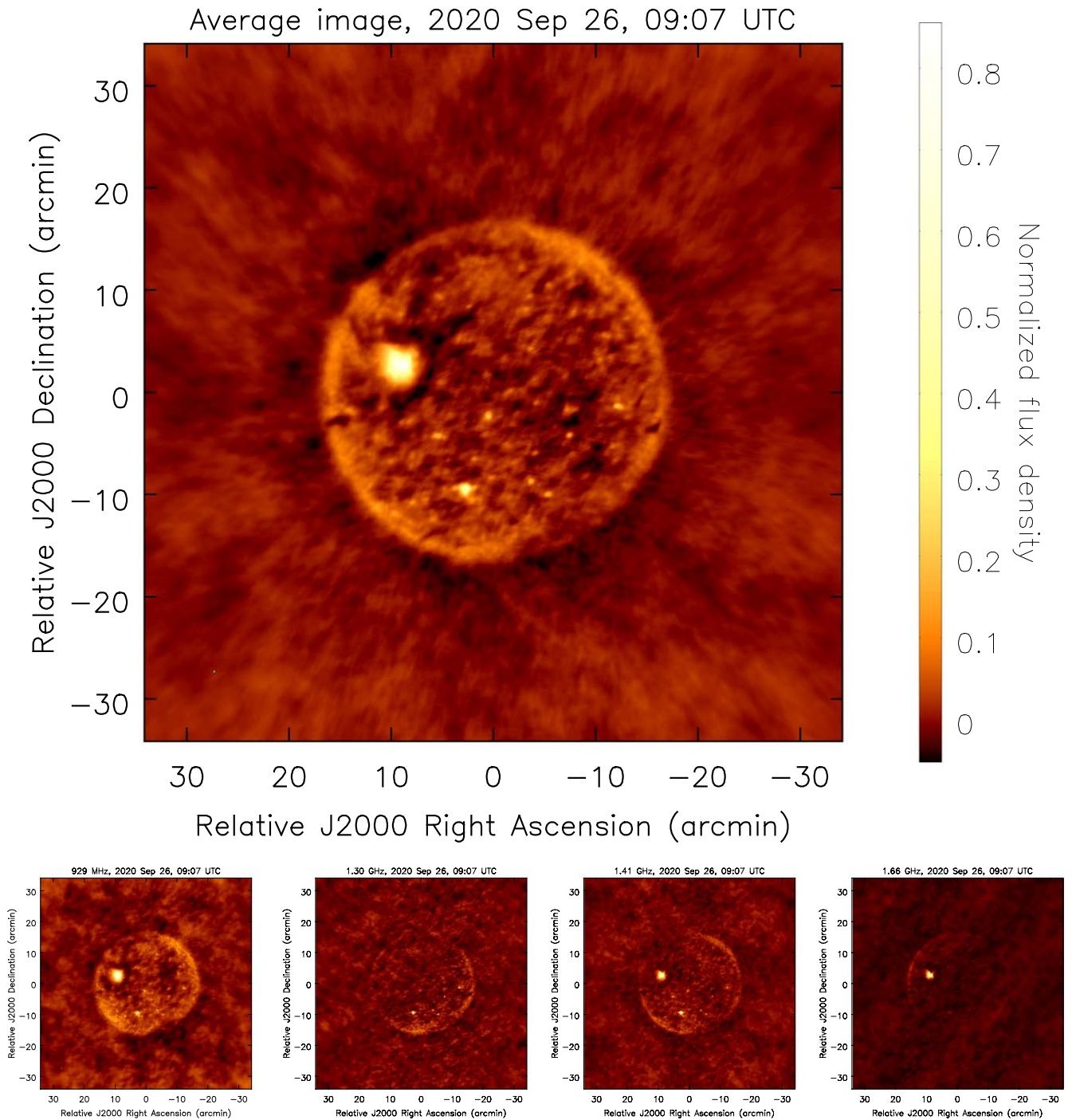


Figure 5. Spectroscopic images of the Sun on 2020 September 26, 09:07 UTC. Top panel: normalized average image over the entire MeerKAT L band. Bottom panels: four sample images at different 20 MHz spectral chunks across the observing band. The small cyan dot at the bottom left represents the PSF of the array.

key aspects of the self-calibration procedure followed here is presented in Appendix B.

3.2. Final Imaging

Once the self-calibration is done, calibration solutions corresponding to the iteration with the maximum DR are applied to the initial calibrated data. We then make final images of the Sun for each spectrottemporal chunk separately using all the baselines. All other imaging parameters—the number of w -layers, visibility weighting, uv -taper, multiscale parameters, and pixel size are kept

the same across the band. During the final imaging, we did not use a predefined mask. Instead, we use the automasking feature available in WSClean to perform deconvolution down to 3σ , where σ is the local rms. Due to the chromatic nature of the primary beam, the low-frequency part of the band has better sensitivity compared to the high-frequency part. At a single spectral slice, the sensitivity also varies across the solar disk due to variations in the primary beam gain over the solar disk. This is evident from the spectral images shown in the bottom panels of Figure 5. At higher frequencies, emissions from the brightest active region are detected with good detection significance, but the

extended emission from the solar limb is not always detected at all frequency chunks. At the same time, at 1.3 GHz even the brightest source corresponding to the active region is not detected because it falls in the null between first and second sidelobes. This is evident from the cyan circle in the top right panel of Figure 2.

It is very interesting to compare the structures detected across the full spectral band with those seen in the simulated radio maps, described later in Section 4.2. The way this is generally done is by averaging in frequency. As we are imaging a very extended source in the sidelobes, the gain of the primary beam varies dramatically across the Sun and the chromaticity of the primary beam leads to large variations across frequency as well. Therefore, correcting for the primary beam in individual spectral slices will lead to averaging of the images with vastly varying spatio-spectral noise characteristics and can degrade the DR with which the emission features are detected. To avoid this issue, for a morphological comparison, we have constructed the spectrally averaged image using images prior to the primary beam correction. We have convolved all images at the resolution of the lowest frequency of the observing band. Then we normalized each 20 MHz spectral image with respect to the peak flux density and averaged all spectral chunks for a given scan to obtain the normalized full-band image shown in the top panel of Figure 5. This normalization ensures that the DR of individual spectral images is maintained while averaging and also ensures that we do not give undue weight to any specific spectral image at any location. The DR of this normalized full-band image integrated over 15 minutes is ~ 500 , which is about an order of magnitude higher than the DR of individual 20 MHz spectral slices.

3.3. Primary Beam Correction and Estimation of the Absolute Flux Density

At lower parts of the band (< 1300 MHz), the Sun was in the first sidelobe of the primary beam, while at the higher frequencies, it was in the second or higher sidelobes, as evident in Figure 2. As the Sun is an extended source the primary beam response also varies across the solar disk. Hence, to obtain the absolute flux density, the direction and frequency dependence of the primary beam need to be corrected.

Holographic measurements of the MeerKAT primary beam (de Villiers & Cotton 2022; de Villiers 2023) at the L band are available¹⁰ over an extent of 4° at an angular resolution of $\sim 223''$. We did linear interpolation to obtain the beam values at each pixel of the image. For alt-az mount telescopes, the sky rotates with respect to the telescope beam, and the rotation angle is known as the parallactic angle (Meadows 2007). If the beam of the instrument is axially symmetric, then parallactic angle correction is not important for Stokes I imaging. As evident from Figure 2, while the main lobe of the MeerKAT primary beam is close to axially symmetric, the same is not true for its sidelobes. In the present observation, the Sun was observed at the sidelobes of the primary beam. Hence, we rotate the primary beam by the parallactic angle before applying the primary beam corrections. We performed an image-plane-based primary beam correction using the array-averaged response. Being at the first/second sidelobe of the primary beam, flux density measurements can have errors due

to the uncertainty in primary beam measurements. Since the observations were done the sidelobes of the primary beam, antenna pointing errors can lead to larger than usual effects. Pointing errors arise when a beam is assumed to be steered precisely toward a certain direction, but in reality, it has a small offset from the desired direction. At present, MeerKAT has an rms pointing error of 0.64 , and no pointing calibration is done for MeerKAT science observations. This would lead to $\sim 5\%$ error in the primary beam power in the sidelobes (de Villiers & Cotton 2022). Considering other kinds of errors (antenna-to-antenna variations in the sidelobes of the primary beam, elevation-dependent effects due to gravity, etc., including the pointing jitters) as discussed in de Villiers (2023), we consider a conservative 10% error on the absolute solar flux density measurements.

To obtain the absolute flux density of the solar emissions, we performed corrections of chromatic primary beam response for each 20 MHz spectral and 15 minute temporal slice individually. Since the primary beam measurements have larger uncertainties at the low primary beam gain regions, for further spectroscopic analysis we have estimated absolute flux density for the spectral points that satisfy the following two conditions:

1. The Sun should not lie beyond the first sidelobe of the primary beam, and the value of the primary beam value toward the Sun should be > 0.001 of the peak.
2. The emission should be detected at a level $> 5\sigma$, where σ is the rms noise of the primary beam corrected image measured very close to the Sun.

4. Results

In this section, we present the results from spectroscopic solar imaging with MeerKAT and compare them with simulated MeerKAT solar maps at frequencies spanning our observations at the L band.

4.1. Spectroscopic Solar Images Using MeerKAT

The spectroscopic images of the Sun made using MeerKAT L -band observations on 2020 September 26 and 2020 September 27 are shown in Figures 5 and 6, respectively. The top panel shows the averaged image over the entire MeerKAT L band following the procedure described in Section 3.2 and the lower panels show four sample spectroscopic images at individual 20 MHz spectral bands spanning the full observing band. The entire solar disk is visible once images over the full band are stacked together. We find that the solar disk is detected at $\sim 50\sigma$ detection, where σ is the rms noise close to the Sun. The diameter of the solar disk is found to be $\sim 35'$, which is slightly larger than the optical disk. MeerKAT images are overlaid on 193 Å images from the Atmospheric Imaging Assembly (AIA) on board the Solar Dynamics Observatory (SDO; Lemen et al. 2012) in Figure 7. The largest active region is colocated with the brightest radio source in MeerKAT images. There are multiple small bright points visible in the AIA image, which are also detected in MeerKAT images with high significance. In both of these images, the diffuse quiet Sun emission from both limbs is also detected with good significance. Although visually both the images show features similar to those seen in the AIA images, we go further to verify this via a comparison with the corresponding simulated solar radio images.

¹⁰ MeerKAT holographic measurements of the primary beam (<https://skafrica.atlassian.net/wiki/spaces/ESDKB/pages/1481572357/The+MeerKAT+primary+beam#A-note-on-sidelobes>).

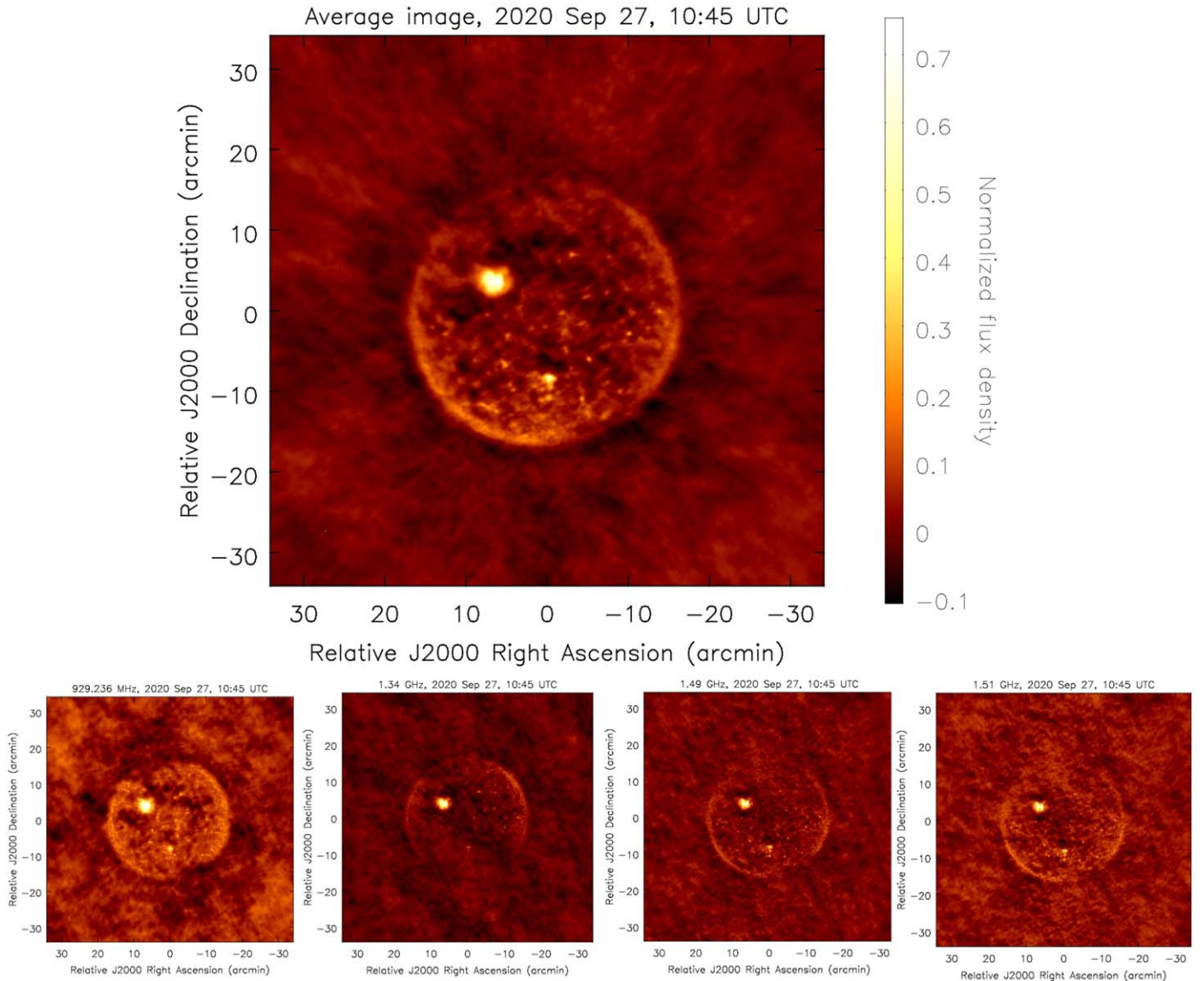


Figure 6. Top panel: normalized average image over the entire MeerKAT L band centered at the time on 2020 September 27, 10:45 UTC. Bottom panels: images at different 20 MHz spectral chunks across the L band. The small cyan dot at the bottom left represents the PSF of the array.

4.2. Simulating Solar Radio Images and Spectra

The simulated images only aim to capture the thermal free-free emission. To generate simulated images, a differential emission measure (DEM) inversion is performed using images at different extreme ultraviolet wavelengths from the AIA/SDO. To reduce the computation time and improve the signal-to-noise ratio (S/N) of the obtained DEMs, the AIA images were smoothed to a resolution of $4''.8$, before DEM inversion. Though this degrades the resolution of these images, the resulting resolution is still finer than that of MeerKAT radio images. Following Hannah & Kontar (2012, 2013), we use the output of the publicly available code¹¹ to compute the expected free-free emission using the code developed by Fleishman et al. (2021). This simulation explicitly considers free-free optical depth of multithermal plasma while performing the radiative transfer calculations. A uniform line-of-sight depth of 100 Mm is assumed through the image. A chromospheric

contribution has also been included, assuming that it is proportional to observations at 304 \AA . The proportionality constant is determined assuming that the chromospheric contribution to the total brightness temperature is 10,880 K (Zirin et al. 1991).

The left panel of Figure 8 shows the simulated T_B map of the Sun at 1.07 GHz and the right panel shows the same map smoothed at MeerKAT angular resolution. It is evident from these figures that there are emissions at a range of angular scales from instrumental resolution to the size of the solar disk. We note that the simulation does not incorporate any propagation effects such as scattering or refraction. While their importance is well established, taking these into account appropriately is beyond the scope of this work.

4.3. Comparing Simulated MeerKAT Images and Observations

Radio interferometry is a Fourier imaging technique, where each baseline of the interferometer measures one Fourier component of the radio sky. Hence, the quality of the images

¹¹ <https://github.com/ianan/demreg/tree/master/python>

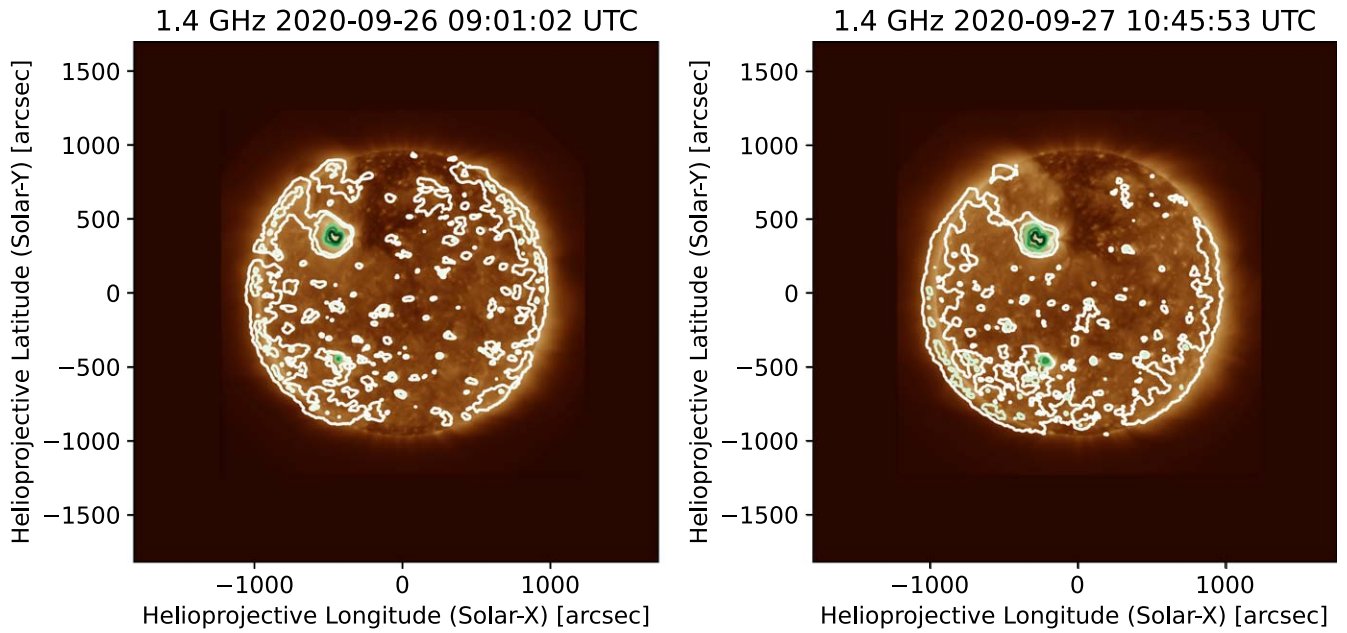


Figure 7. MeerKAT solar images overlaid on AIA/SDO 193 Å images. Left panel: image on 2020 September 26, 09:07 UTC. Contours are at 4%, 10%, 40%, 60%, and 80% of the peak flux density. Right panel: image on 2020 September 27, 10:45 UTC. Contours are at 7%, 20%, 40%, 60%, and 80% of the peak flux density. In both images, there are no noise peaks at the lowest contour level over a region $\sim 1 \times 1$ deg. The lowest contours in both images are chosen at the 20σ level, where σ is the measured rms close to the Sun.

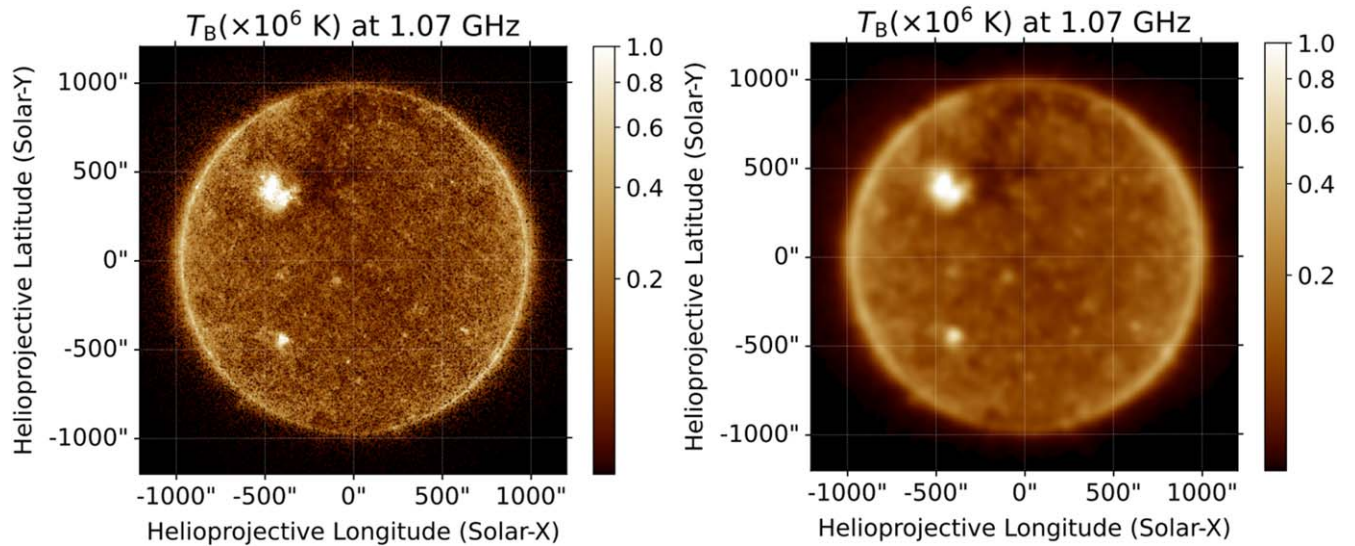


Figure 8. Simulated radio map on 2020 September 26, 09:06 UTC. Left panel: simulated radio map of the Sun at 1.07 GHz at a pixel scale of $4''/8$. Right panel: the same image is convolved with the PSF of the observation at 1 GHz ($\sim 8''$).

and the scales of emission captured rely crucially on the sampling of the Fourier plane achieved by the interferometric observations. To build the appropriate simulated image for comparison with the observed MeerKAT images, we first create simulated visibilities from the simulated images using the MeerKAT array configuration and observing parameters used for these observations. These visibilities are then inverted to make the synthetic MeerKAT radio image that would have been observed by MeerKAT.

A comparison between the synthetic MeerKAT image thus obtained and the observed MeerKAT image at the same time is shown in Figure 9. The left panel shows the synthetic MeerKAT map and the right panel shows the observed map

from MeerKAT. The similarities between the simulated and observed images are very evident. The most striking similarities are the locations and relative intensities of the various bright points; some of them have been marked by cyan circles in both panels of the same figure. There are also differences, the prominent ones are the presence of noise in the regions beyond the Sun, the limb being not as bright and well defined in the MeerKAT image as compared to the synthetic image, and the differences in the details of the morphology of the brightest active region. While the first of these can be attributed to the combined effect of the thermal noise associated with the image, the imperfections in the calibration and imaging process along with scattering in the solar atmosphere, may also play a role.

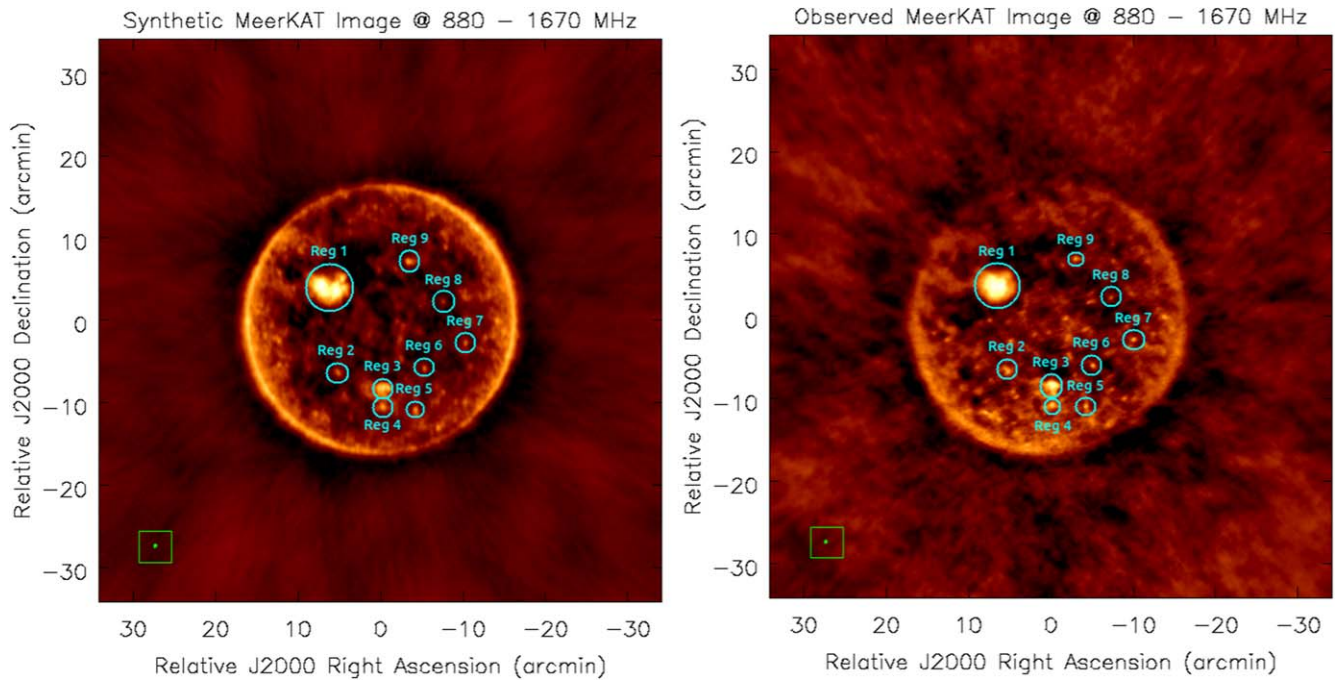


Figure 9. Comparison between synthetic and observed MeerKAT radio images on 2020 September 27, 10:45 UTC. Left panel: synthetic MeerKAT solar radio image. Right panel: observed MeerKAT solar radio image. Both images are made using the entire frequency range from 880–1670 MHz. In both images, multiple bright regions have been detected. Some of them are marked by cyan circles. Small green-filled circles at the bottom left corner marked by a green box represent the PSF of the images.

4.4. Comparison of Observed and Simulated Spectra

In this section, we compare observed spectra with the expected spectra from the simulated images. Absolute flux density calibration is done following the method described in Section 3.3 before extracting the spectra. We have extracted spectra for two bright active regions present on the Sun, which are marked by red and green circles in the top panel of Figure 10, which is in the unit of brightness temperature. Corresponding brightness temperature spectra from these MeerKAT images for regions 1 and 2 are shown by the filled circles in the bottom left panel of Figure 10. The criteria for points to be used for estimating absolute flux density were laid down in Section 3.3 and are met only below 1070 MHz. This limits the span of the spectra shown here.

We have extracted spectra of these two regions from the corresponding simulated radio maps (one sample simulated spectral map is shown in the left panel of Figure 8), which are shown by solid lines in the left bottom panel of Figure 10. Observed values shown by filled circles in the same figure are significantly different from the simulated values. We note that the simulation describes a rather ideal situation and can differ from observations due to several reasons, including the following:

1. Simulation assumes the thermal free–free emission from the coronal plasma to be the only emission mechanism in operation. In reality, however, the emission would be a superposition of the thermal free–free emission and gyrosynchrotron/gyroresonance emission at these frequencies (Nindos 2020).
2. The simulation ignores any propagation effects, while in reality refraction and scattering can lead to discernible effects.

3. Interferometers are sensitive only to the brightness distributions at certain angular scales and not to a constant background. This implies that interferometers tend to not be sensitive to emissions at large angular scales. The details of the largest angular scale to which an array is sensitive depend upon the details of the array configuration and the sampling of the Fourier domain achieved by the observation under study. This can lead to a reduction in the observed flux density when compared to the simulated values.

It is feasible to isolate the impact of the last possibility mentioned above. To do this, we generate synthetic spectral maps of the Sun for MeerKAT array configuration as described in Section 4.3, which can be compared directly with the observed MeerKAT solar maps for an apples-to-apples comparison. The spectra from these synthetic simulated maps are shown by unfilled diamonds in the bottom left panel of Figure 10. The spectra from synthetic maps are consistent with those from the observations. This demonstrates that the large discrepancy between the observed and simulated spectra (shown by solid lines in the same figure) is primarily due to the missing flux density in MeerKAT solar maps. The ratio of the flux density measured in the observed map to that in the simulated map is defined to be missing flux density fraction and is plotted in the bottom right panel of Figure 10. The red circle at the center of the uv -plane shown in Figure 1 corresponds to the uv -cell for a source with the size of the solar disk of $32'$ in angular scale. There is no uv -sampling in that cell. Hence, it is expected to have missing flux for the Sun for the MeerKAT array configuration.

The missing flux density fraction decreases with the decrease in frequency. For a given array layout, one sample with increasingly shorter spacings in the uv -plane with decreasing

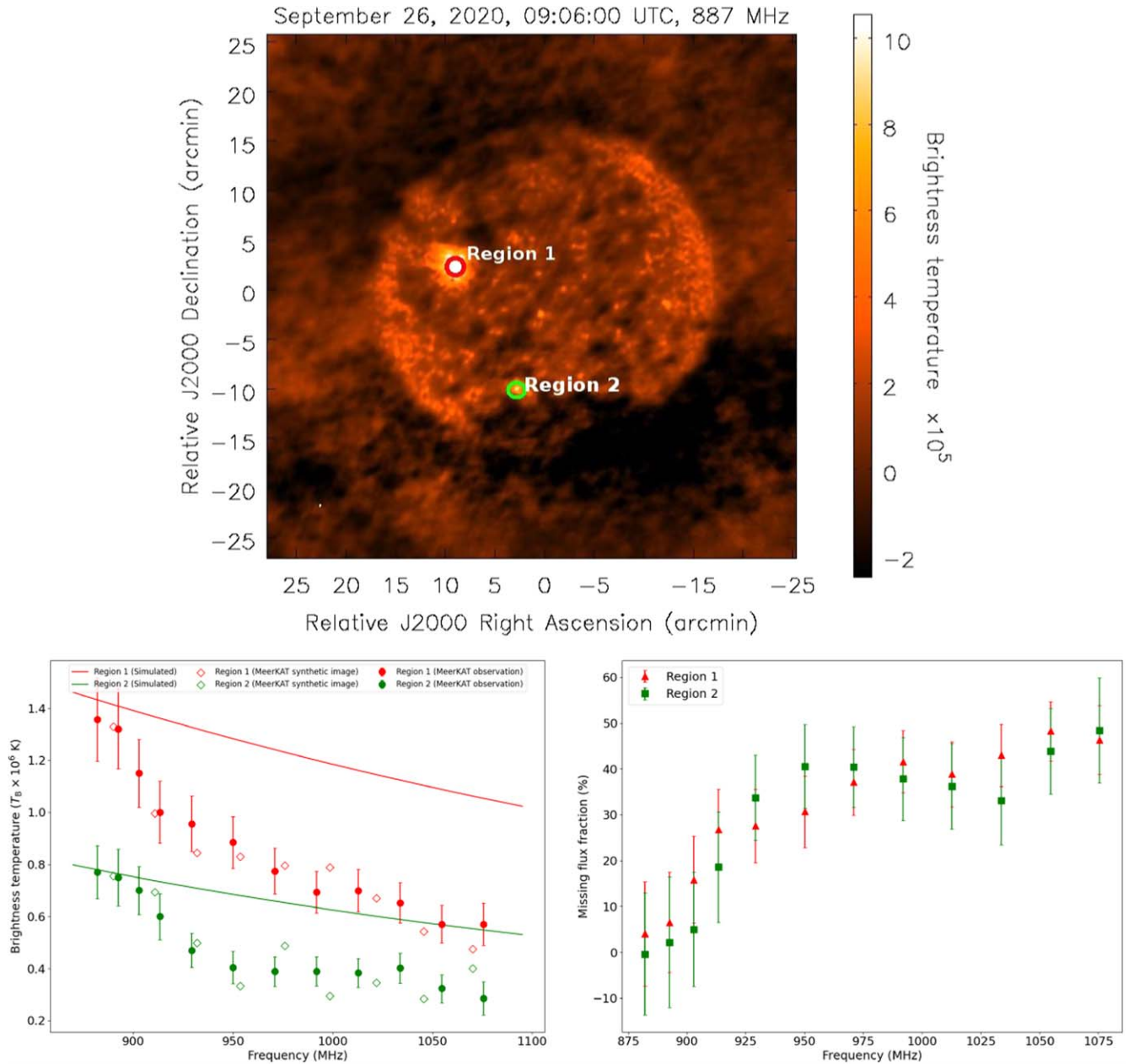


Figure 10. Comparison of observed spectra with simulated spectra. Top panel: a sample observed image at 887 MHz. Two regions are marked by red and green circles where spectra have been extracted. Spectra are extracted over a $20''$ region centered around these regions. Bottom left panel: spectra for regions 1 and 2 are shown in red and green colors, respectively. Solid lines represent the simulated spectra considering thermal emission (one sample image is shown in Figure 8). Unfilled diamonds represent spectra from synthetic MeerKAT maps obtained from the simulation. Filled circles represent the measured spectra from the MeerKAT observation on 2020 September 26. Bottom right panel: missing flux fraction is shown as a function of frequency.

frequency and missing flux density fraction at larger angular scales is expected to drop. The observed variation in the missing flux density fraction shows this trend and substantiates this to be the major cause of the observed differences between the simulated and observed MeerKAT solar spectra. While the other two reasons mentioned above could also be contributing to the observed differences, their effects, however, are smaller than the uncertainty on these measurements.

5. Conclusion and Future Work

The Sun is an extremely complicated radio source with emissions at angular scales ranging from a few arcseconds to the size of the solar disk at gigahertz frequencies, as is evident

from the simulated radio map shown in the left panel of Figure 8. Solar emissions also show rapid spectrottemporal variations. Hence, to study the solar radio emission at gigahertz frequencies, one requires a high-DR and high-fidelity spectroscopic snapshot imaging of the Sun. Sufficiently dense spectroscopic snapshot uv -coverage of MeerKAT allows high-DR and high-quality imaging of the Sun. Solar observation with MeerKAT has not yet been commissioned, and these observations were done keeping the Sun in the sidelobes of the primary beam.

Here, we have presented the first detailed spectroscopic imaging study of the Sun with MeerKAT. Given the well-behaved spectroscopic snapshot PSF and the precise calibration, the images presented here are the highest quality

spectroscopic snapshot solar images at these frequencies available to date. To demonstrate the capability of MeerKAT in producing very high-quality spectroscopic solar images, we have compared MeerKAT images with the synthetic MeerKAT images designed to sample the same Fourier components as MeerKAT observations. The correspondence between the observed and simulated images shown in Figure 9 is remarkable and it is evident from the fact that several weak solar emissions present in the synthetic image are detected with high significance in the MeerKAT image as well.

Although the spatial structures in the observed image match well with the simulated image, from a scientific perspective, it is also important to test the ability of MeerKAT to determine the flux densities and spectra of solar features. As substantiated in Section 4.4, MeerKAT spectra show evidence of missing flux at higher frequencies, which drops to insignificant levels by about 900 MHz. An implication is that while MeerKAT images in the UHF band are not expected to suffer from the missing flux density issue, one will need to be careful about the missing flux density at the L band and higher. A comparison with different regions from the simulated maps radio maps might provide a good way to quantify the missing flux density fraction for specific observations.

While it is adequate for demonstrating the feasibility of MeerKAT for solar observations and evaluating the quality of the images it can deliver, a key limitation of the present observing approach arises from the issues related to imaging a source of large angular size in the chromatic primary beam sidelobes. Since the primary beam gain at the first sidelobe is ~ -30 dB, we lose the sensitivity by a factor of ~ 1000 compared to the observation done using the main lobe of the primary beam. This was however necessitated by the requirement to attenuate the solar signals to a level that would keep the signal chain downstream in its linear regime. Hence, a preferable approach for solar observing will be to keep the Sun in the main lobe of the primary beam and adjust the gains of the appropriate elements of the signal chain to attenuate the signal to the required levels. Some members of this team are currently working with the MeerKAT engineering team to identify the suitable attenuation for solar observations and to develop a calibration strategy for solar observations performed along these lines. Once enabled, we are convinced that, with its high-quality spectroscopic snapshot solar imaging capability, MeerKAT solar observations will open a new frontier in solar radio physics.

Acknowledgments

MeerKAT telescope is operated by the South African Radio Astronomy Observatory, which is a facility of the National Research Foundation, an agency of the Department of Science and Innovation. The authors acknowledge the contribution of all those who designed and built the MeerKAT instrument. We also thank the anonymous referee for the comments and suggestions that helped improve the clarity and presentation of this work. We thank Sharmila Goedhart and Fernando Camilo for their comments on an earlier draft of the manuscript, which helped improve its technical correctness. We also thank the MeerKAT team for their assistance. D.K. and D.O. acknowledge the support of the Department of Atomic Energy, Government of India, under project No. 12-R&D-TFR-5.02-0700. D.K. thanks Barnali Das (CSIRO, Australia) for the

useful comments on the manuscript. This research has made use of NASA’s Astrophysics Data System (ADS).

Facilities: MeerKAT, SDO.

Software: astropy (Astropy Collaboration et al. 2013; Price-Whelan et al. 2018; Astropy Collaboration et al. 2022), matplotlib (Hunter 2007), NumPy (Harris et al. 2020), CASA (McMullin et al. 2007; The CASA Team et al. 2022), WSClean (Offringa et al. 2014).

Appendix

Here, we discuss the analysis steps followed in some detail, with an emphasis on self-calibration.

Appendix A Initial Flagging and Calibration

We performed flagging and calibration using CASA (The CASA Team et al. 2022). We have used J0408-6545 as the flux density calibrator for both epochs and its model is described in the MeerKAT calibration manual.¹² The flagging and calibration of the flux density and phase calibrators essentially follow the standard iterative procedure as indicated in the blocks marked by green and blue, respectively, in Figure 3. For solar scans, only the data with zero amplitudes, known bad spectral channels, and bad antennas were flagged. No automated flagging was performed on uncalibrated solar scans.

Being a non-sidereal source, the equatorial coordinates of the Sun change with time. To accommodate this, we treated each 15 minute solar scan independently for self-calibration and imaging. We also did not consider the full spectral range simultaneously during self-calibration and imaging because both the solar flux density and the primary beam gains in the sidelobes vary significantly with frequency. Hence, after applying the initial calibration solutions obtained toward the pointing center, we split every 15 minute solar scan into 20 MHz spectral chunks for self-calibration and imaging.

Appendix B Self-calibration

Although the Sun is in the sidelobes of the primary beam, it is still the source with the highest flux density contributing to the observed visibilities. Before primary beam correction, the next brightest source in the field has a flux density of 38 mJy beam^{-1} , while the peak flux density on the Sun is about 1.7 Jy beam^{-1} . The total integrated flux density of background sources is about 0.5 Jy , whereas the integrated flux density of the Sun is about 15 Jy . Since the total contribution from background sources is only about 3.3%, they do not affect the self-calibration significantly.

As the Sun is present about 2.5° away from the pointing center, gain solutions toward the Sun may be different from those determined toward the pointing center. To estimate and correct the complex gains toward the direction of the Sun, we first shifted the phase center of the visibilities to the center of the Sun for each solar scan and then performed self-calibration on each spectral chunk of every scan separately. This has been done to account for the chromatic primary beam response and also the spectral variations in emissions from solar structures.

¹² J0408-6545 model (<https://skafrica.atlassian.net/wiki/spaces/ESDKB/pages/1452146701/L-band+gain+calibrators>).

Another major challenge in self-calibrating solar observation is the large variation in the flux distribution across baselines of varying lengths. Assuming the Sun to be a uniformly illuminated disk of size $32'$, the first null of the visibility amplitude distribution lies close to 100λ , and the amplitudes of visibilities for baselines less than 100λ increase very rapidly as one moves toward shorter baselines. Hence, one needs good uv -coverage at baseline lengths $<100\lambda$ to properly model this emission. However, there are a limited number of short baselines of length $\leq 100\lambda$ at MeerKAT for L -band observations. To avoid issues arising due to sparse uv -coverage at $\leq 100\lambda$, we only use baselines $>100\lambda$ during the self-calibration.











We followed the following self-calibration steps:

1. First, we make a circular mask of diameter $35'$ centered at the Sun.
2. An image is made using WSClean from the calibrated data using antenna gain solutions obtained from flux density and phase calibrators. We choose baselines $>100\lambda$ and use Briggs weighting (Briggs 1995) with robustness 0^{13} along with a circular taper at $19\text{ k}\lambda$.
3. We keep w -stacking on, and the number of w -planes is chosen automatically by WSClean.
4. Deconvolution is performed using the mask centered on the Sun. The average rms (σ) close to the Sun is about 0.1 Jy and we performed deconvolution down to 3σ , 0.3 Jy . We used multiscale deconvolution with Gaussian scale sizes $0, 5, 9, 15, 25$, and 35 times the pixel size, where one pixel is chosen to be of $1''$.
5. The deconvolved model of the Sun is converted into model visibilities using WSClean and used for self-calibration.
6. We performed four rounds of phase-only self-calibration followed by five rounds of amplitude-phase self-calibration. Time-dependent gain solutions are calculated using the CASA task `gaincal` at a 1 minute time interval using `solmode=L1R` and `minsnr=3`, using baselines $>100\lambda$.
7. Due to sidelobe response, visibility amplitudes for two parallel-hand polarizations (XX and YY) could be different. Hence, during the amplitude-phase self-calibration, we make separate sky models for the XX and YY polarizations.
8. Since some antennas, the ones with primarily long baselines, may not have a sufficient S/N for performing self-calibration, time-dependent gain solutions are applied using the `applycal` task of CASA in the `calonly` mode to retain the long baseline antennas with the initial calibration solutions.

We have calculated the DR of the spectral images as the ratio of peak solar flux density and the measured rms close to the Sun. The change in DR with self-calibration iterations is shown in Figure 4. When the DR of three consecutive self-calibration rounds does not change by more than 1, we consider the self-calibration to have converged. Once phase-only self-calibration has converged, we move to amplitude-phase self-calibration. We noticed there is an increase in DR by about 20% when amplitude-phase self-calibration is initiated. Once the amplitude-phase self-calibration has also converged, the self-calibration loop is stopped. Though the improvements in DR with self-calibration iterations were comparatively modest, the final images shown in Figure 5 do not show any significant deconvolution artifacts, implying that good calibration has been achieved.

¹³ Definition of robustness parameter as per WSClean (https://wsclean.readthedocs.io/en/latest/image_weighting.html).

ORCID iDs

Devojoyoti Kansabanik  <https://orcid.org/0000-0001-8801-9635>
 Surajit Mondal  <https://orcid.org/0000-0002-2325-5298>
 Divya Omeroi  <https://orcid.org/0000-0002-4768-9058>
 James O. Chibueze  <https://orcid.org/0000-0002-9875-7436>
 N. E. Engelbrecht  <https://orcid.org/0000-0003-3659-7956>
 R. D. Strauss  <https://orcid.org/0000-0002-0205-0808>
 E. P. Kontar  <https://orcid.org/0000-0002-8078-0902>
 G. J. J. Botha  <https://orcid.org/0000-0002-5915-697X>
 P. J. Steyn  <https://orcid.org/0000-0003-2099-8093>
 Amoré E. Nel  <https://orcid.org/0000-0001-6917-1105>

References

- Astropy Collaboration, Price-Whelan, A. M., & Lim, P. L. 2022, *ApJ*, **935**, 167
 Astropy Collaboration, Robitaille, T. P., Tollerud, E. J., et al. 2013, *A&A*, **558**, A33
 Briand, C., Ceconi, B., Chrysaphi, N., et al. 2022, *URSL*, **4**, 17
 Briggs, D. S. 1995, AAS Meeting, **187**, 112.02
 Chen, W., Barr, E., Karuppusamy, R., Kramer, M., & Stappers, B. 2021, *JAI*, **10**, 2150013
 de Villiers, M. S. 2023, *AJ*, **165**, 78
 de Villiers, M. S., & Cotton, W. D. 2022, *AJ*, **163**, 135
 Dewdney, P. E., Braun, R., & Turner, W. 2017, in 2017 32nd General Assembly and Scientific Symp. of the Int. Union of Radio Science (URSI GASS) (Piscataway, NJ: IEEE)
 Fleishman, G. D., Kuznetsov, A. A., & Landi, E. 2021, *ApJ*, **914**, 52
 Fox, N. J. 2017, AGUFM, **2017**, SH 21C-02
 García Marirrodriga, C., Pacros, A., Strandmoe, S., et al. 2021, *A&A*, **646**, A121
 Gary, D. E. 2023, *ARA&A*, **61**, 427
 Gary, D. E., Nita, G. M., & Sane, N. 2012, AAS Meeting, **220**, 204.30
 Hallinan, G., Anderson, M., Isella, A., et al. 2023, AAS Meeting, **241**, 451.09
 Hannah, I. G., & Kontar, E. P. 2012, *A&A*, **539**, A146
 Hannah, I. G., & Kontar, E. P. 2013, *A&A*, **553**, A10
 Harris, C. R., Millman, K. J., van der Walt, S. J., et al. 2020, *Natur*, **585**, 357
 Heywood, I., Rammala, I., Camilo, F., et al. 2022, *ApJ*, **925**, 165
 Hunter, J. D. 2007, *CSE*, **9**, 90
 Jonas, J. & MeerKAT Team 2016, in Proc. of Science 277, MeerKAT Science: On the Pathway to the SKA, ed. R. Taylor (Trieste: SISSA), 1
 Kassim, N., White, S., Rodriguez, P., et al. 2010, in Proc. of the Advanced Maui Optical and Space Surveillance Technologies Conf., ed. S. Ryan (Kihei, HI: The Maui Economic Development Board), E59
 Lemen, J. R., Title, A. M., Akin, D. J., et al. 2012, *SoPh*, **275**, 17
 Lonsdale, C. J., Cappallo, R. J., Morales, M. F., et al. 2009, *IEEEP*, **97**, 1497
 McMullin, J. P., Waters, B., Schiebel, D., Young, W., & Golap, K. 2007, in ASP Conf. Ser. 376, Astronomical Data Analysis Software and Systems XVI, ed. R. A. Shaw, F. Hill, & D. J. Bell (San Francisco, CA: ASP), 127
 Meadows, P. 2007, *JBAA*, **117**, 35
 Müller, D., St. Cyr, O. C., Zouganelis, I., et al. 2020, *A&A*, **642**, A1
 Nakariakov, V., Bisi, M. M., Browning, P. K., et al. 2015, in Proc. of Science 215, Advancing Astrophysics with the Square Kilometre Array (AASKA14), ed. R. Braun et al. (Trieste: SISSA), 169
 Nindos, A. 2020, *FrASS*, **7**, 57
 Nindos, A., Kontar, E. P., & Omeroi, D. 2019, *AdSpR*, **63**, 1404
 Nindos, A., Patsourakos, S., Alissandrakis, C. E., & Bastian, T. S. 2021, *A&A*, **652**, A92
 Omeroi, D., Bisoi, S. K., Sasikumar Raja, K., et al. 2023, *JApA*, **44**, 40
 Offringa, A. R., McKinley, B., Hurley-Walker, N., et al. 2014, *MNRAS*, **444**, 606
 Pick, M., & Vilmer, N. 2008, *A&ARv*, **16**, 1
 Price-Whelan, A. M., Sipőcz, B., Günther, H., et al. 2018, *AJ*, **156**, 123
 Raouafi, N. E., Matteini, L., Squire, J., et al. 2023, *SSRv*, **219**, 8
 Rast, M. P., Bello González, N., Bellot Rubio, L., et al. 2021, *SoPh*, **296**, 70
 Reber, G. 1944, *ApJ*, **100**, 279
 Rimmele, T. R., Warner, M., Keil, S. L., et al. 2020, *SoPh*, **295**, 172
 Santander-Vela, J., Bartolini, M., Miccolis, M., & Rees, N. 2021, arXiv:2110.13329
 The CASA Team, Bean, B., Bhatnagar, S., et al. 2022, *PASP*, **134**, 114501
 Tingay, S. J., Goetze, R., Bowman, J. D., et al. 2013, *PASA*, **30**, e007
 van Haarlem, M. P., Wise, M. W., Gunst, A. W., et al. 2013, *A&A*, **556**, A2
 Wayth, R. B., Tingay, S. J., Trott, C. M., et al. 2018, *PASA*, **35**, e033
 Zarka, P., Coffre, A., Denis, L., et al. 2018, in 2018 2nd URSI Atlantic Radio Science Meeting (AT-RASC) (Piscataway, NJ: IEEE)
 Zirin, H., Baumert, B. M., & Hurford, G. J. 1991, *ApJ*, **370**, 779